https://doi.org/10.1016/j.ijplas.2018.10.013

Interactive effect of stress state and grain size on fracture behaviours of copper in micro-scaled plastic deformation

W.T. Li[a, b], H. Li[c], M.W. Fu[a, b, *]

[a] PolyU Shenzhen Research Institute, No. 18 Yuexing Road, Nanshan District, Shenzhen, PR China

[b] Department of Mechanical Engineering, The Hong Kong Polytechnic University, Kowloon, Hong Kong, PR China

[c] State Key Laboratory of Solidification Processing, School of Materials Science & Engineering, Northwestern Polytechnical University, Xi'an, 710072, China

* E-mail: mmmwfu@polyu.edu.hk

ABSTRACT: To explore the interactive influence of the deformation stress state and material microstructural grain size on the fracture behaviour in micro-scaled deformation, a series of micro-scale copper specimens of various geometrical dimensions and microstructural grain sizes are prepared and deformed to achieve various stress states represented by stress-related variables, such as the normalised third deviatoric stress invariant and the stress triaxiality. The speckle pattern method of continuous tracking is used to investigate the mechanical responses of materials in various deformation stress states and material microstructures, and a finite-element simulation of each deformation is conducted with the combined surface layer and grain boundary strengthening constitutive model, which considers the contributions of the surface grain, grain interior and grain boundary in representing the grain and geometry sizes. The interactive effects of the normalised third invariant, stress triaxiality and microstructural grain size on the fracture strain are identified and established by accounting for the correlation between the results of simulation and those of physical experimentation. Their influences on the fracture mechanism, mode and behaviour are further explored. The results reveal that greater stress decreases the fracture strain in the tensile deformation of round bar and cylindrical compression and increases the fracture strain in sheet shear and tensile deformations. The larger grain size generates fewer micro-voids, more uneven grain distribution and severer localisation deformation, which accelerates failure. Furthermore, stress triaxiality and the normalised third invariant at a low stress triaxiality are decreased with the increase of grain size, which in turn affects the occurrence of fracture. These effects coexist and compete with each other. In view of these influences, a larger grain size and a higher stress state inhibit the occurrence of fracture for sheet specimens with fracture modes from shear-dominant to dimple-dominant; in contrast, a smaller grain size and a lower stress state inhibit the occurrence of fracture in other cases.

Keywords: Grain size; Stress state; Ductile fracture; Combined constitutive model; Fracture mechanism

1. Introduction

Ductile fracture is a pivotal phenomenon that cannot be ignored in product fabrication and service. In product fabrication, ductile fracture influences the formability of materials and the quality of the product in deformation-based manufacturing. Ductile fracture can occur in product service due to severe loading conditions and poor structural quality and deteriorate the load-carrying capacity of products and their performance, leading to disastrous consequences in product service. For micro-scale products, ductile fracture is more critical in the product development and service stages because it is more difficult to explore and understand. Product miniaturisation has become a strong tendency. Increasing numbers of quality micro-scale parts and components must be manufactured for use in various industrial clusters such as micro-electro-mechanical systems, electronic devices and biomedical instruments (Fu and Chan, 2012; Fu et al., 2016; Vollertsen et al., 2009). The development of a systematic knowledge system to support the development and service of micro-product has become more crucial than ever before.

Ductile fracture must therefore be considered and extensively explored in product manufacturing and service. The formation micro-mechanism of fracture initiation, which covers micro-defects nucleation, growth and coalescence, is considered to be a primary mechanism in the early formation of ductile fracture in macro-scale deformation (Gurson, 1977; McClintock et al., 1966; Puttick, 1959). In this process, the equivalent plastic strain, the stress triaxiality and the normalised third deviatoric stress invariant (or the Lode parameter related to the normalised third invariant) are key influential factors in the occurrence of ductile fracture (Bai and Wierzbicki, 2008; Brünig et al., 2018; Gao et al., 2009; Lou and Huh, 2013; Lou et al., 2012; Teng et al., 2017; Wierzbicki et al., 2005). Ductile fracture in micro-scale deformation (μ-deformation), however, becomes more complicated when the occurrence of size effects, mainly in the formats of grain and geometry size effects, is considered (Ban et al., 2017; Keller and Hug, 2017; Kim et al., 2007; Meng et al., 2015; Ran et al., 2013; Xu et al., 2015b). Size effect is referred to as the variation of physical behaviours or phenomena of the concerned structures and materials that arises from the value changes of size effect parameters.

To examine the thickness effect on the tension properties of miniature sheets, Yang and Lu (2013) conduct tensile experiments with various thick copper specimens with fine and coarse grains. Their results revealed that a critical ratio exists between thickness and grain size and that below this critical value, the work-hardening coefficient, uniform elongation and tensile strength of sheets with different grain sizes are reduced with decreasing thickness. In addition, the specimen with a fine grain has a larger critical value. When the ratio of thickness to grain size is lower, the scatter effect of mechanical property is noticeable, and the fracture mode of sheet metal changes from normal tensile fracture to pure shear fracture, as reported by Zhang and Dong (2016). In micro-compression, Xu et al. (2015a) investigate the grain and geometry size effects on surface roughening and mechanical behaviour. A larger grain size and a smaller sample size lead to more obvious surface roughening effect and lower flow stress. Furushima et al. (2014) revealed that free surface roughening affects the failure of metal foil. During the plastic deformation of metal foil, free surface roughening that causes an increase in surface roughness can be observed. Local deformation occurs more easily at the concave region resulting from greater surface roughness, and fracture thus forms at a low fracture strain. Furthermore, Zhang et al. (2018) compared the surface profiles of deformed sheet specimens with fine, medium and coarse grains and showed that thickness has a significant influence on surface roughening when the specimen has a ratio of thickness to grain size below three, whilst it has little effect on surface roughening in the case of values above six. These studies assessed size effects on the deformation behaviour, fracture mode and mechanism.

To better predict the fracture formation in μ-deformation, some researchers have combined size effect parameters into fracture criteria developed at the macro-scale. Ran et al. (2013) proposed a surface layer model with a size factor and combined it with the Freudenthal fracture criterion to forecast the fracture initiation in samples with various grain and geometry sizes in μ-deformation with flanged upsetting. The prediction of the model based on size effect is more accurate than the conventional model. Xu et al. (2015b) explored the effects of grain and geometry size on the voids' nucleation, growth and coalescence and introduced different scale factors into the Gurson-Tvergaard-Needleman and Thomason models to construct forming limit curves (FLC). The predicted FLC and physical experiments show good agreement. Size effects should thus be considered in micro-scale ductile fracture.

The fracture strain of materials in macro-scaled plastic deformation strongly depends on the deformation stress state, which has been well established and explored in many studies. Bao and Wierzbicki (2004) found that the equivalent strain to fracture is reduced when the stress triaxiality is increased in the cases of tensile and compressive experiments with round bar specimens, whilst the opposite observation was made in shear and tensile experiments with flat specimens. Zhang et al. (2001) revealed that Lode parameter strongly affects the voids' shape and the stress and strain distribution in voids' coalescence. The Lode parameter is thus another crucial factor, in addition to stress triaxiality, that should not be neglected in the investigation of ductile fracture, especially in deformations with stress triaxiality at negative or low values, because they have a noticeable influence on void evolution (Barsoum and Faleskog, 2007a, b; Brünig et al., 2013). Considering the Lode parameter and stress triaxiality as stress state variables to characterise the accumulation of damage in deformation, Bai and Wierzbicki (2008) assumed a 3D fracture locus in which the influence of stress triaxiality on fracture strain is represented as a parabolic function and the effect of Lode angle parameter on fracture strain is represented as an exponential function. This new fracture locus was validated. To model fracture formation, Lou and Huh (2013) represented the nucleation, growth and coalescence of voids with the equivalent plastic strain, stress triaxiality and the Lode parameter, respectively. The criterion based on this modelling approach can predict the likelihood that sheets will fail in various stress states using DP980 steel. According to these earlier studies of the roles played by the Lode parameter and stress triaxiality in macro-scaled ductile fracture, the correlations amongst size effect, the Lode parameter and stress triaxiality demand thorough exploration to allow a clear understanding of ductile fracture in μ-deformation.

In addition to the influence of the stress state on fracture behaviour, the fracture mode and micro-mechanism are also affected. Barsoum and Faleskog (2007b) concluded that fracture surfaces are characterised by large and deep dimples under high stress triaxiality, and small and elongated shear dimples with low stress triaxiality. The final ruptures are caused by the internal void necking and shearing mechanisms, respectively. Li et al. (2011) showed that the maximum principal stress-dominant deformation occurs in the round bar tensile experiments and dimple fracture thus dominates at high stress triaxiality. In compressive experiments, shear fracture occurs in a spot with negative stress triaxiality and shear-dominant deformation. For places with low stress triaxiality between the two ranges described above, mixed shear and dimple fractures develop under the combination of the maximum principal stress-dominant and shear-dominant deformations. However, the influence of the stress state on macro-scale and meso-scale ductile fracture is their focus, and the interactive influence of the stress state and grain size on ductile fracture in μ-deformation remains unclear, especially for the stress state in the range from negative to positive.

This study thus aims to investigate the interactive effect of the deformation stress state and the material microstructural grain size on fracture behaviour in μ-deformation, which is represented by the normalised third deviatoric stress invariant, stress triaxiality, grain size and fracture strain, based on micro-scale tension, shear and compression deformations, and to further explore the influences of the stress state and grain size on the mechanism, mode and behaviour of fracture. To obtain various stress state variables, 11 pure copper specimens of various geometrical shapes are designed and annealed under different conditions to achieve various grain sizes. According to the metallographs of these specimens, the area ratios of surface grain (SG), grain interior (GI) and grain boundary (GB) are determined with ArcMap software via digital image technology. The extracted information and the true stress and strain responses of micro-scale cylinder, dog-bone and smooth bar specimens are used to determine the parameters of the combined constitutive model developed by Li et al. (2017) in the corresponding deformations. The mechanical behaviour calculated by the corresponding model is then input to ABAQUS software to simulate the various deformation processes. The load-displacement responses of simulation and physical experiments of samples with various grain sizes and geometrical dimensions are compared to validate the combined model in different deformation modes. The interactive influence between the stress state and the grain size on fracture strain is thus recognised and understood based on the physical experiments and simulated results. Furthermore, the effects of grain size and stress state on the mechanism, mode and behaviour of fracture are analysed by observation of scanning electron microscope (SEM) fractographs. Our study thus advances the understanding of ductile fracture in μ-deformation and further facilitates the development of related knowledge.

2. Combined constitutive model

The combined constitutive model was proposed in our previous study, in which the contributions of SG, GI and GB to the flow stress of material are designated as follows (Li et al., 2017):

$$\begin{cases} \sigma(\varepsilon) = f_{\mathrm{surf}} \mathrm{m} \tau_{\mathrm{R}}(\varepsilon) + f_{\mathrm{gb}}(\sigma_{\mathrm{y}}^{\mathrm{gb}} + \mathrm{np} + \mathrm{h_{gb}} \varepsilon^{\mathrm{n_{gb}}}) + f_{\mathrm{gi}}(\sigma_{\mathrm{y}}^{\infty(\mathrm{gi})} + \mathrm{k} d^{-1/2} + (\mathrm{h}_{\mathrm{gi}}^{\infty} + \mathrm{a} d^{-1/2}) \varepsilon^{\mathrm{n_{gi}}}) \\ 1 = f_{\mathrm{surf}} + f_{\mathrm{gb}} + f_{\mathrm{gi}} \end{cases} \tag{1}$$

where $\sigma(\varepsilon)$ and ε are the flow stress and strain of the material, respectively, and f_{surf}, f_{gb} and f_{gi} are the fractions of SG, GB and GI, respectively; $\tau_{\mathrm{R}}(\varepsilon)$ and m are the critical resolved shear stress and the orientation factor, respectively (Kim et al., 2007); $\sigma_{\mathrm{y}}^{\mathrm{gb}}$ is the yield stress of the grain boundary; n, $\mathrm{h_{gb}}$ and $\mathrm{n_{gb}}$ are the material constants of the grain boundary; $\mathrm{p} = -\frac{1}{3}(\sigma_1 + \sigma_2 + \sigma_3)$ is the hydrostatic pressure; σ_1, σ_2 and σ_3 are the first, second and third principal stresses, respectively; $\sigma_y^{\infty(gi)}$, k, h_{gi}^{∞} and a are also material constants in the case of single crystals; n_{gi} is the work hardening exponent of the grain interior, and *d* is the grain size.

Fig. 1 illustrates the material composition. The surface layer model shows that SG is positioned at the outer layer and the inner grain is located at the inner part of the material. The flow stresses of SG and the inner grain are represented by the flow stresses of single crystal and polycrystal, respectively, mainly due to their similar flow stresses in the mixed surface layer model developed by Lai et al. (2008) and Peng et al. (2009), as displayed in Eq. (2). Meyersm and Ashworth (1982) reported that GB and GI are two parts of the polycrystalline aggregate. The strength of the inner grain approximates that of polycrystalline aggregate and can thus be formulated with the grain boundary strengthening model widely used by Jiang and Weng (2004a, 2004b) and by Zhou et al. (2008), in which the flow stresses of GB and GI are represented by Eq. (3). Hence, the specimen material represented by the combined model is composed of SG, GB and GI, and the mechanical behaviour of material in this study consists of these three parts.

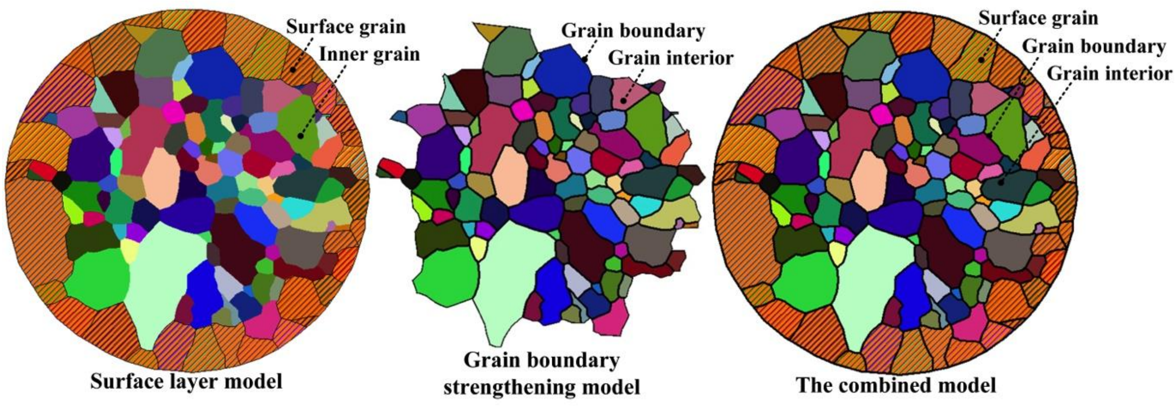

Fig. 1 The material composition in different models.

$$\begin{cases} \sigma(\varepsilon) = f_{\mathrm{surf}} \mathrm{m}\tau_{\mathrm{R}}(\varepsilon) + f_{\mathrm{inner}}(\mathrm{M}\tau_{\mathrm{R}}(\varepsilon) + \mathrm{K}(\varepsilon) d^{-1/2}) \\ 1 = f_{\mathrm{surf}} + f_{\mathrm{inner}} \end{cases} \tag{2}$$

where the strengths of SG and the inner grain are $\sigma_{surf}(\varepsilon) = m\tau_R(\varepsilon)$ and $\sigma_{inner}(\varepsilon) = M\tau_R(\varepsilon) + K(\varepsilon)d^{-1/2}$, respectively. $M\tau_R(\varepsilon)$ and $K(\varepsilon)$ are constants for a given strain ε. M is an orientation factor with values of 3.06 and 2.23, for face centred cubic crystals in the Taylor and Sachs models, respectively (Clausen et al., 1998).

$$\begin{cases} \sigma_{poly}(\varepsilon) = f_{gb}(\sigma_y^{gb} + np + h_{gb}\varepsilon^{n_{gb}}) + f_{gi}(\sigma_y^{\infty(gi)} + kd^{-1/2} + (h_{gi}^{\infty} + ad^{-1/2})\varepsilon^{n_{gi}}) \\ 1 = f_{gb} + f_{gi} \end{cases} \quad (3)$$

In Eq. (3), the strengths of polycrystalline aggregate, GB and GI are $\sigma_{poly}(\varepsilon)$, $\sigma_{gb}(\varepsilon) = \sigma_y^{gb} + np + h_{gb}\varepsilon^{n_{gb}}$ and $\sigma_{gi}(\varepsilon) = \sigma_y^{\infty(gi)} + kd^{-1/2} + (h_{gi}^{\infty} + ad^{-1/2})\varepsilon^{n_{gi}}$, respectively.

3. Micro-scale experiments

3.1 Specimen preparation and experimental setup

Fig. 2 shows the 11 specimens made of pure copper, including four cylindrical and seven round and sheet specimens, that are used to obtain various stress states in meso-scale and micro-scale compression and tension experiments. Fig. 3 presents their various microstructures. Four compression specimens are annealed at 835, 845 and 875 °C for 1 h in an environment of high-purity argon, and their microstructures are shown in Figs. 3(a) to (c). Four sheet specimens are annealed at 400, 600 and 750 °C for 1 h, and their microstructures are given in Figs. 3(d) to (f). Three round bar tension specimens are annealed at 400, 750 and 1000 °C for 3, 1 and 1 h, respectively, and their microstructures are illustrated in Figs. 3(g) to (i). These specimens are annealed to obtain different grain sizes and to weaken the texture of copper. According to Chan et al. (2012), a high annealing temperature significantly weakens the texture of copper. Meng et al. (2018) investigated the relationship of plastic anisotropy and the number of grains across the thickness direction of stainless steel foil and reported that when the number of grains across thickness direction is above the critical value of 4, the property of material can be considered as homogeneous and viewed as isotropy in macroscopic scale. In Fig. 3, the number of grains across the thickness or diameter direction for most specimens is much larger than 4. It is thus assumed that the texture of the annealed copper does not have a significant effect on the material property.

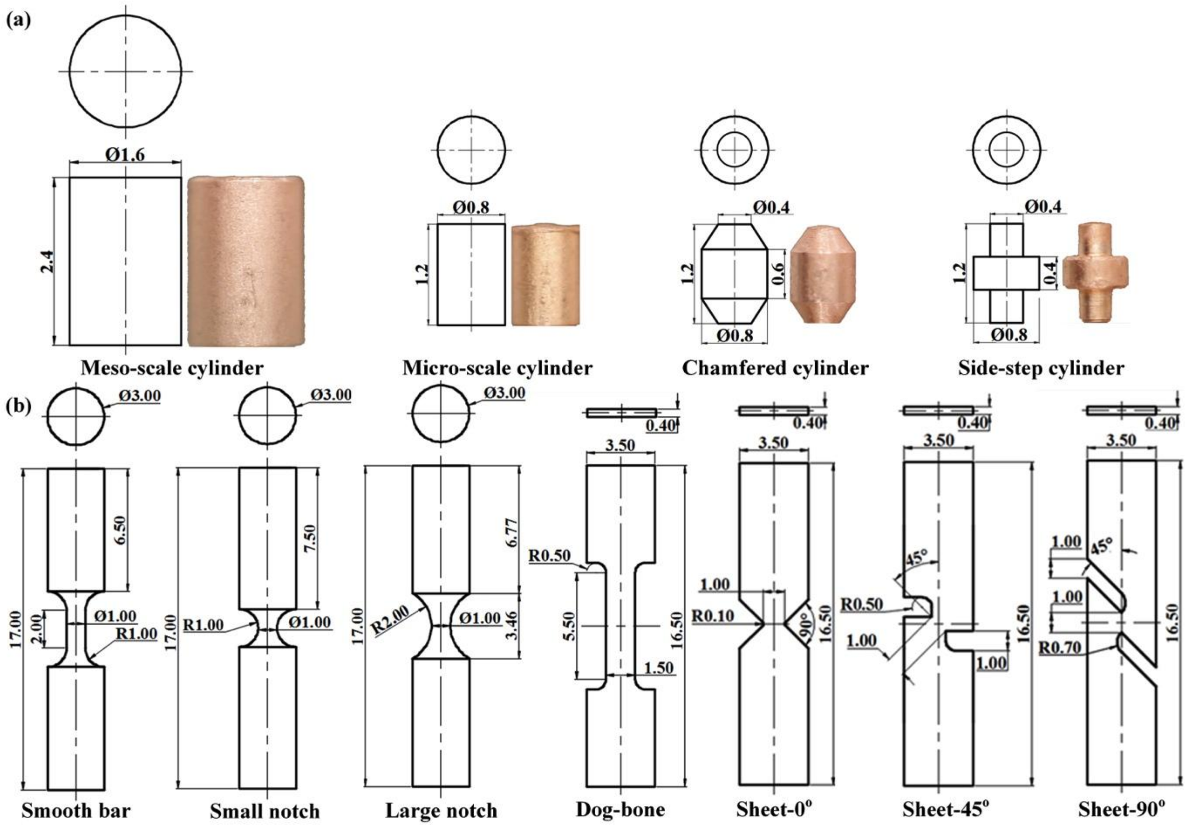

Fig. 2 Specimen designs. (a) Compression; (b) Tension and shear samples (Dimensions in mm).

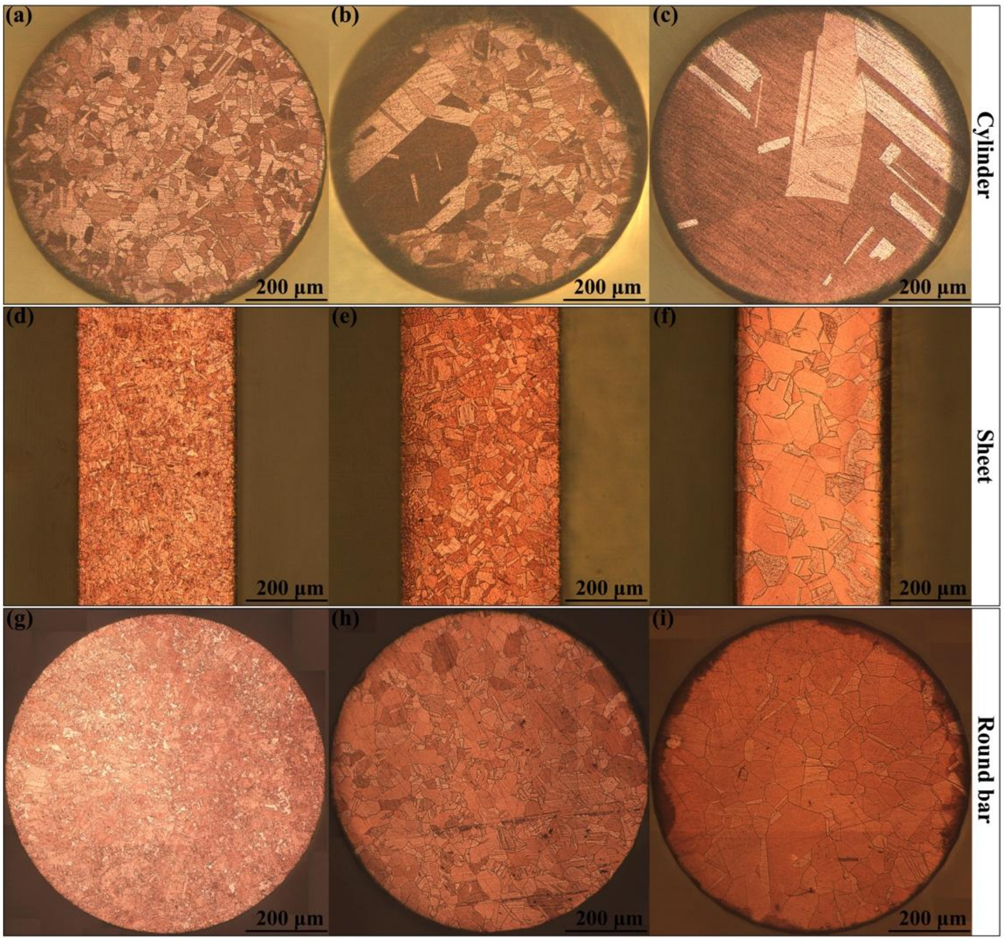

Fig. 3 Metallographs of copper samples annealed at (a) (835 °C, 1 hour); (b) (845, 1); (c) (875, 1); (d) (400, 1); (e) (600, 1); (f) (750, 1); (g) (400, 3); (h) (750, 1); and (i) (1000, 1).

Fig. 4(a) shows the complete micro-scale compression process recorded by a digital camera in a fixed time interval. In this process, macro-scale cracks are not obvious on the circumferential surface, whilst micro-scale cracks on the equatorial area of the compressed specimen can be observed on SEM fractograph. It is difficult to carry out the micro-scale tension experiments with miniature sheet and round bar specimens under the universal grips mainly because of small dimensions. Two sets of micro-scale grips are uniquely designed and fabricated to facilitate the experiments. One for round bar specimens is displayed in Fig. 4(b) and the other for sheet is similar except the dimensions which match cross sections of specimens, as shown in Fig. 4(c). The load and displacement in the physical experiments are measured and used to obtain the specimens' true stress and strain relationships.

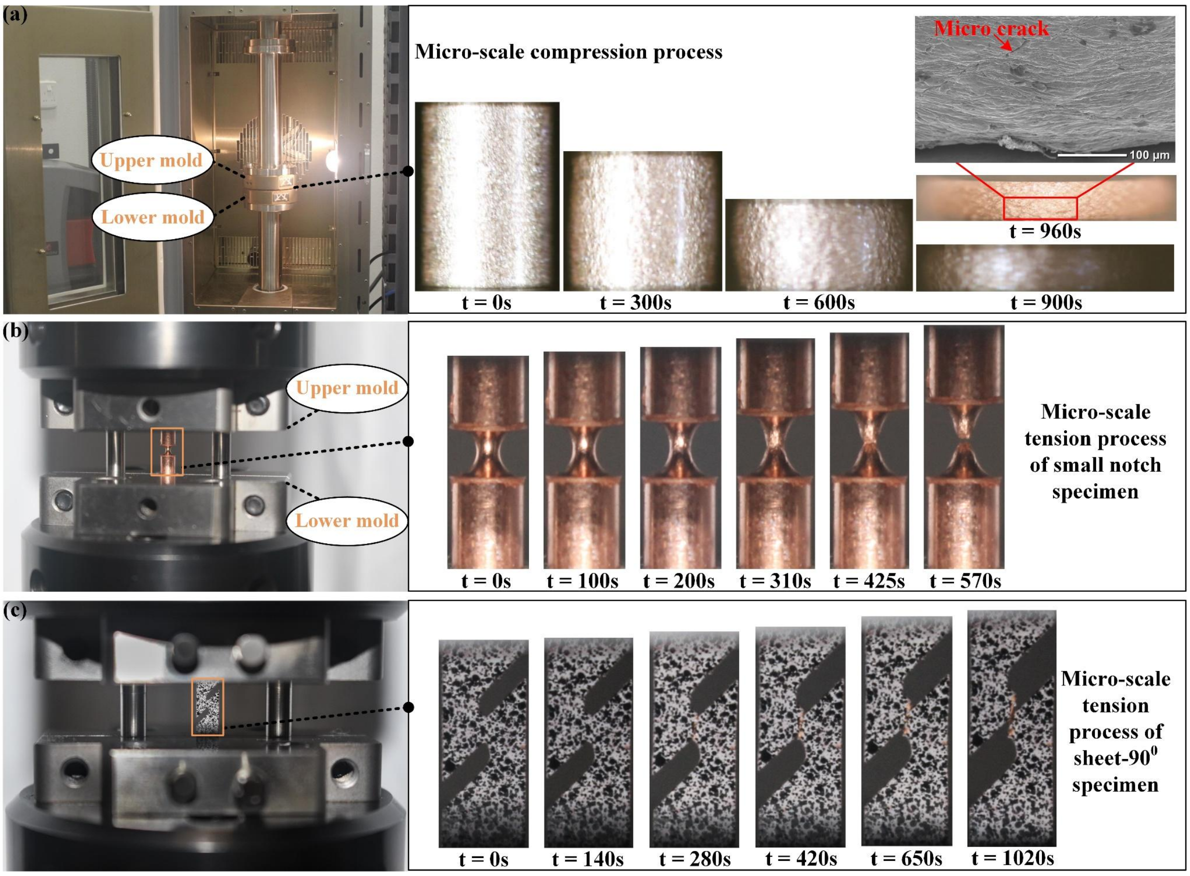

Fig. 4 Micro-scale experiments. (a) Compression; (b) Tension with round bar; and (c) Tension with sheet.

3.2 Digital image processing

The area fractions of SG, GB and GI in the metallograph are identified with ArcMap software via digital image processing. Fig. 5 illustrates schematically the method used to identify the three parts of material, in which each picture is regarded as a raster layer and converted to the editable points, polylines and polygons. GB is first identified by setting a specific threshold for each metallograph. Complete extraction of the GB is usually difficult due to problems with the quality of the metallograph, such as overly localised oxidation and low contrast. The successful extraction of GB can thus be realised via automatic and manual digitalisation. The total raster layer characterised by SG, GI and GB is obtained with the algorithm function by converting the editable polygon layer of GB into the raster layer in ArcMap. The raster layer of SG can be identified in the same manner. Finally, the results that differentiate SG, GI and GB are obtained and displayed in Fig. 5. Therefore, the area ratios of these three portions are established by summarising the area of pixels in the corresponding raster layer. Table 1 presents the mean grain sizes and area ratios of SG, GB and GI for various specimens.

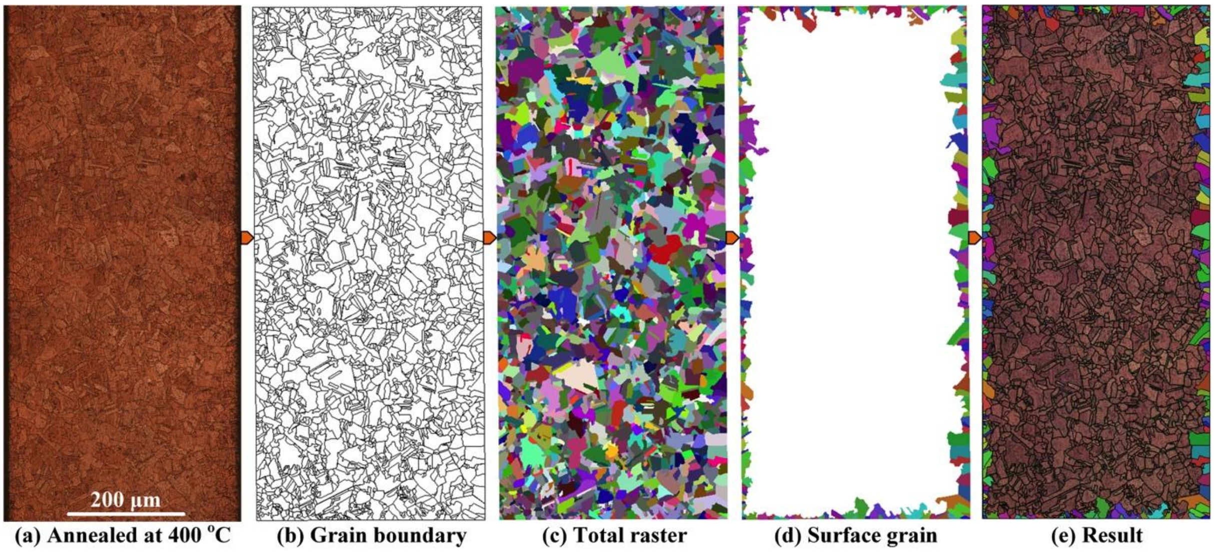

Fig. 5 Schematic diagrams for differentiating SG, GB and GI.

Table 1 Area fractions of SG, GB and GI for various specimens.

Specimens	Annealing (°C + h)	f_{surf} (%)	f_{gb} (%)	f_{gi} (%)	d (μm)
Cylinder	835 + 1	20.36	4.86	74.78	24.31
	845 + 1	43.06	2.99	53.95	52.08
	875 + 1	96.35	0.79	2.86	206.57
Sheet	400 + 1	10.58	6.90	82.52	12.2
	600 + 1	17.88	5.12	77.00	45.07
	750 + 1	40.18	2.21	57.61	110.1
Round bar	400 + 3	2.8	23.06	74.14	8.23
	750 + 1	19.93	8.85	71.22	41.78
	1000 + 1	32.78	4.17	63.05	79.36

3.3 Parameter determination in the combined model

In this study, the detailed values of three sets of parameters in the combined model are determined based on the true stress and strain relationships of various specimens to represent their mechanical responses in compression and tension experiments. The method by which the parameters are determined according to the flow strengths of micro-scale cylinders with various grain sizes is described below.

First, the true stresses and grain sizes of micro-scale cylinders are fitted linearly in the Hall-Petch function when true strain is constant, as exhibited in Fig. 6(a). Each value of $\mathrm{M}\tau_\mathrm{R}(\varepsilon)$ is determined for the corresponding strain designated in Fig. 6(b). A non-linear fitting function is thus established for $\mathrm{M}\tau_\mathrm{R}$ and ε, as designated in Eq. (4):

$$\mathrm{M}\tau_\mathrm{R}(\varepsilon) = 361.23\varepsilon^{0.36} \tag{4}$$

In accordance with the fitting results, the flow stress of the SG is formulated with Eq. (5) by adopting 3.06 and 2 for M and m, respectively, in the following:

$$\sigma_\mathrm{surf}(\varepsilon) = \mathrm{m}\tau_\mathrm{R}(\varepsilon) = 236.1\varepsilon^{0.36} \tag{5}$$

Second, the average grain size and the area ratios of SG, GB and GI, viz. d, f_surf, f_gb and f_gi are presented in Table 1 based on the microstructural analysis. To obtain the parameters in the flow strengths of GB and GI, n is assumed to be 0.4, according to Zhou et al. (2008). Based on the true stress and strain responses of specimens with three different grain sizes, $\sigma_\mathrm{y}^{\infty(\mathrm{gi})}$, k, and $\sigma_\mathrm{y}^\mathrm{gb}$ are then determined when the strain is zero. Last, the non-linear curve fitting method is used to determine the remaining parameters $\mathrm{h}_\mathrm{gi}^\infty$, h_gb, a, n_gi and n_gb. The flow strengths of GB and GI are determined and formulated in Eqs. (6) and (7), as follows:

$$\sigma_\mathrm{gb}(\varepsilon) = 76.75 + 0.4\mathrm{p} + 3880\varepsilon^{0.28} \tag{6}$$

$$\sigma_\mathrm{gi}(\varepsilon) = 36.98 - 174.07d^{-1/2} + (238 + 62.07d^{-1/2})\varepsilon^{0.28} \tag{7}$$

The combined constitutive models are thus established and designated in Eqs. (8) to (10) in the following, using the method described above to model the mechanical properties of cylindrical, sheet and round bar specimens, respectively.

$$\begin{cases} \sigma(\varepsilon) = f_{\mathrm{surf}} 236.1\varepsilon^{0.36} + f_{\mathrm{gb}}(76.75 + 0.4\mathrm{p} + 3880\varepsilon^{0.28}) \\ \qquad + f_{\mathrm{gi}}\left(36.98 - 174.07d^{-1/2} + (238 + 62.07d^{-1/2})\varepsilon^{0.28}\right) \\ 1 = f_{\mathrm{surf}} + f_{\mathrm{gb}} + f_{\mathrm{gi}} \end{cases} \tag{8}$$

$$\begin{cases} \sigma(\varepsilon) = f_{\mathrm{surf}} 551.49\varepsilon^{0.95} + f_{\mathrm{gb}}(450 + 0.4\mathrm{p} + 0.02\varepsilon^{0.9}) \\ \qquad + f_{\mathrm{gi}}\left(- 14.15 + 309.87d^{-1/2} + (447.9 + 0.01d^{-1/2})\varepsilon^{0.4}\right) \\ 1 = f_{\mathrm{surf}} + f_{\mathrm{gb}} + f_{\mathrm{gi}} \end{cases} \tag{9}$$

$$\begin{cases} \sigma(\varepsilon) = f_{\mathrm{surf}} 391.86\varepsilon^{0.535} + f_{\mathrm{gb}}(16.91 + 0.4\mathrm{p} + 815.99\varepsilon^{0.47}) \\ \qquad + f_{\mathrm{gi}}\left(10.57 - 1.21d^{-1/2} + (629.01 + 3.56d^{-1/2})\varepsilon^{0.47}\right) \\ 1 = f_{\mathrm{surf}} + f_{\mathrm{gb}} + f_{\mathrm{gi}} \end{cases} \tag{10}$$

Fig. 7 indicates that the experimental and fitted stress and strain curves generated with the samples of meso-scale and micro-scale cylinders, dog-bone and smooth bar with various grain sizes show good agreement. In addition, it can be seen from Fig. 7(c) that the accuracy of the combined model with smooth bar is better than that of Ran's model (Ran et al., 2013), especially for the sample with a larger grain size (Li et al., 2017).

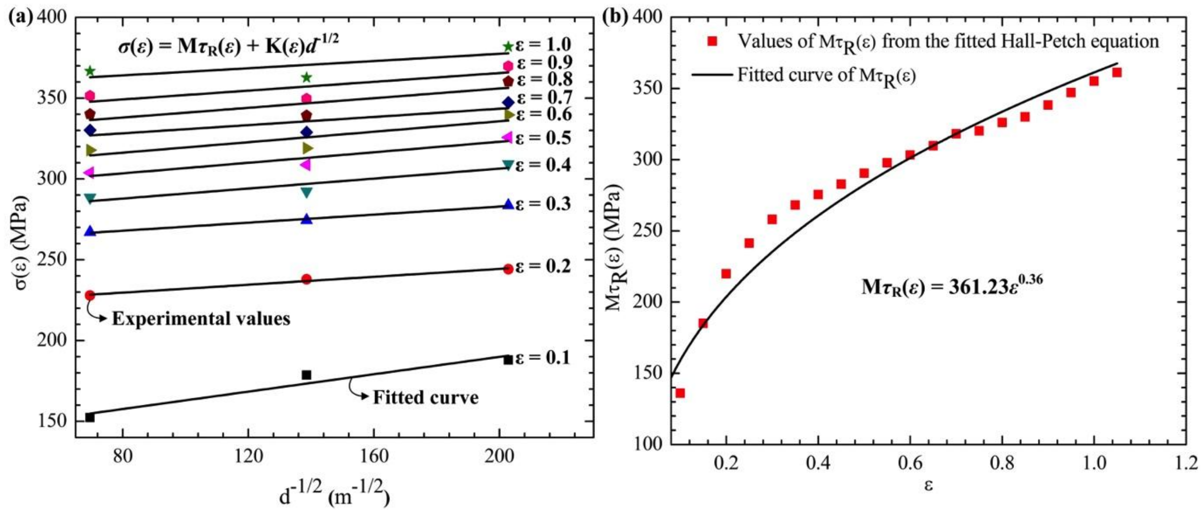

Fig. 6 The fitted curves for the micro-scale cylinder. (a) The Hall-Petch relationship; and (b) $M\tau_R(\varepsilon)$ equation.

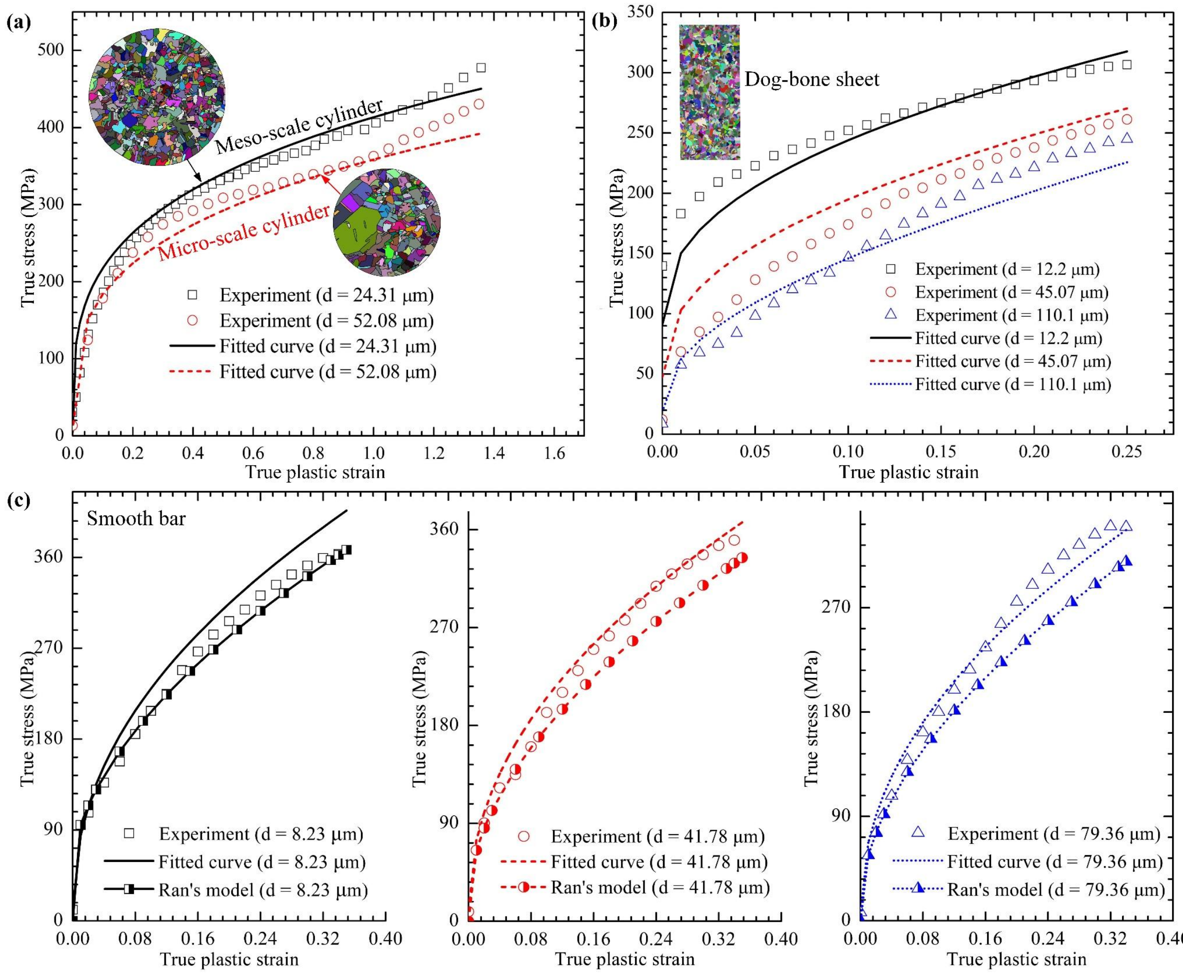

Fig. 7 The experimental and fitted stress and strain curves with various grain sizes. (a) Cylinders; (b) Dog-bone sheet; and (c) Smooth bar (Li et al., 2017).

4. Results and discussion

4.1 Numerical and experimental results

For the specimens of sheet-0°, sheet-45° and sheet-90°, the speckle pattern method of continuous tracking is used to obtain the displacement according to the object-oriented tracking model proposed by Zhu et al. (2016). To begin, white and black paints are sprayed onto the specimen as the background and the random speckle patterns, respectively. These speckles in black are viewed as multiple objects. A series of images taken during plastic deformation are then imported into a database system, PostgreSQL, to track the multiple objects and compute the displacement at each time step. Fig. 8 shows the tracking process of sheet-0° specimen. First, a specific threshold is given for each image, and each black speckle is extracted as a set of spatially contiguous pixels. These pixels are then converted into a polygon with an enclosed boundary to be modelled as an object, as shown in Fig. 8(b). As the time interval is very short for each pair of consecutive images, polygons of the same object in two consecutive time steps show significant and exclusive overlapping. Whenever significant overlap is obtained, a pair of polygons are determined as the two consecutive states of the same object. Thus, the objects with a time series of polygons are constructed, and the movement locus of each object during the complete micro-scale tension experiment is shown in Fig. 8(c). Fig. 8(d) illustrates the movement locus of objects in different time steps. Different colours mean different time. Fig. 8(e) gives the movement locus of objects based on different polygons. Different colours refer to different polygons. Fig. 8(f) presents the movement locus of objects with a time series of polygons. Different colours mean different objects. After tracking is finished, the two-dimensional coordinate of the central point of each polygon is recorded. Finally, the displacements of these speckle patterns at each time step are computed.

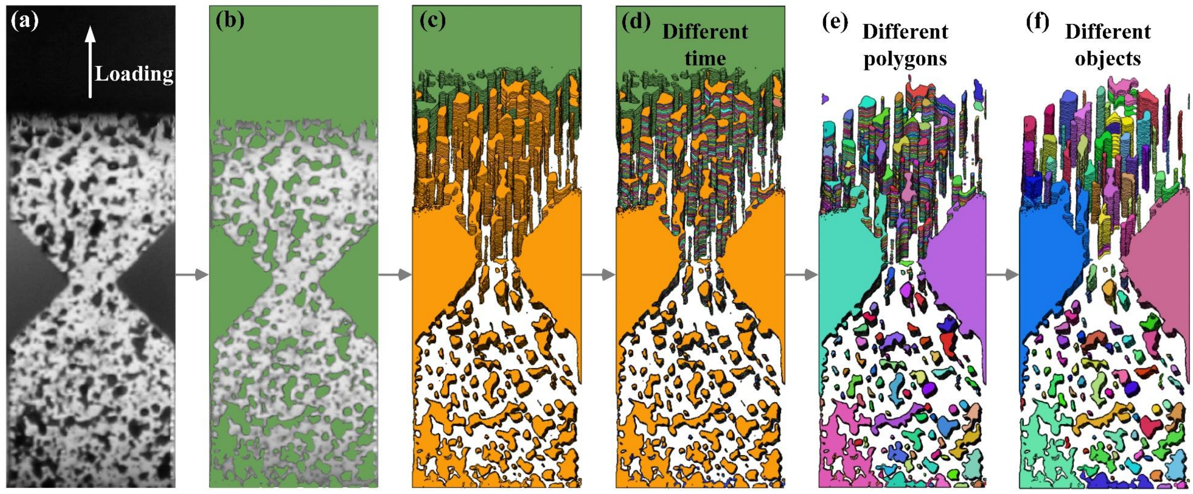

Fig. 8 The process of continuous tracking speckle patterns. (a) Reference image; (b) Objects in the reference image; (c) The movement locus of objects in a time series of images taken during the complete micro-scale tension experiment; (d) Visualisation based on different time; (e) Visualisation based on different polygons; and (f) Visualisation based on different objects with a time series of polygons.

Furthermore, each deformation is simulated with the finite-element software Abaqus/Explicit. The bar and cylinder specimens are modelled as four-node bilinear axisymmetric elements (CAX4R), whilst the sheet specimens are modelled as reduced integration first-order solid elements (C3D8R). The typical meshes in the geometrical shape transition regions of chamfered cylinder, sheet-0^0 and small notch specimens are illustrated in Fig. 9. The experimental load and displacement responses in the micro-scale compression, shear and tension experiments are compared with the results of the simulations using the combined model designated in Eqs. (8) to (10). Figs. 10 to 12 show the correlation of the simulated load-displacement curves and the physical experiments with specimens of various grain sizes and geometries in the compression and tension experiments. The results show good agreement. Although deviation is seen for certain specimens, the variation trend is similar. The deviation between the load-displacement response of simulation and the physical experiments mainly results from the deviation between the true stress-strain response and the value fitted by the combined model. The combined model is thus validated in various deformation modes.

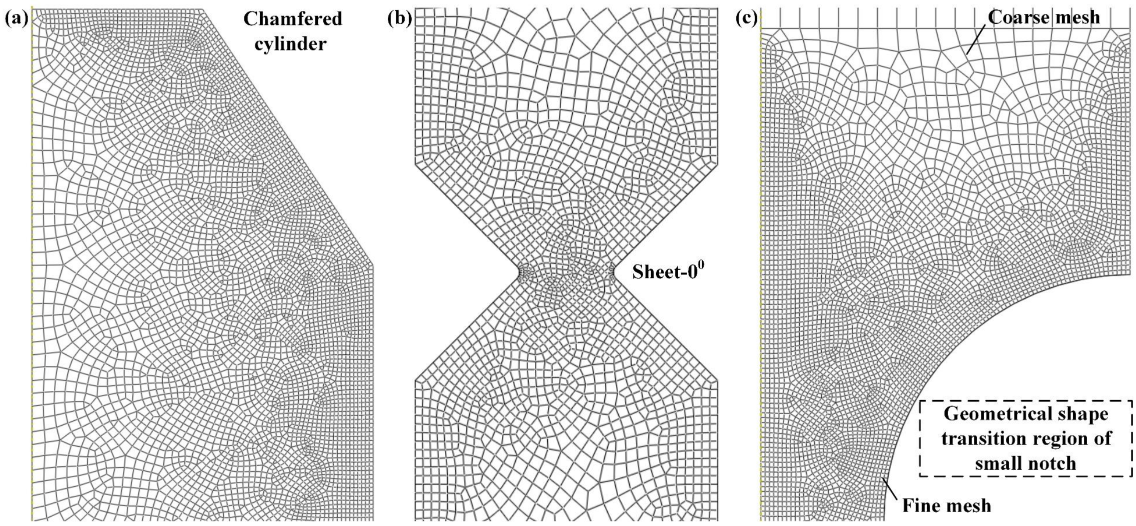

Fig. 9 Typical meshes in the geometrical shape transition regions of specimens. (a) Chamfered cylinder; (b) Sheet-0^0; and (c) Small notch.

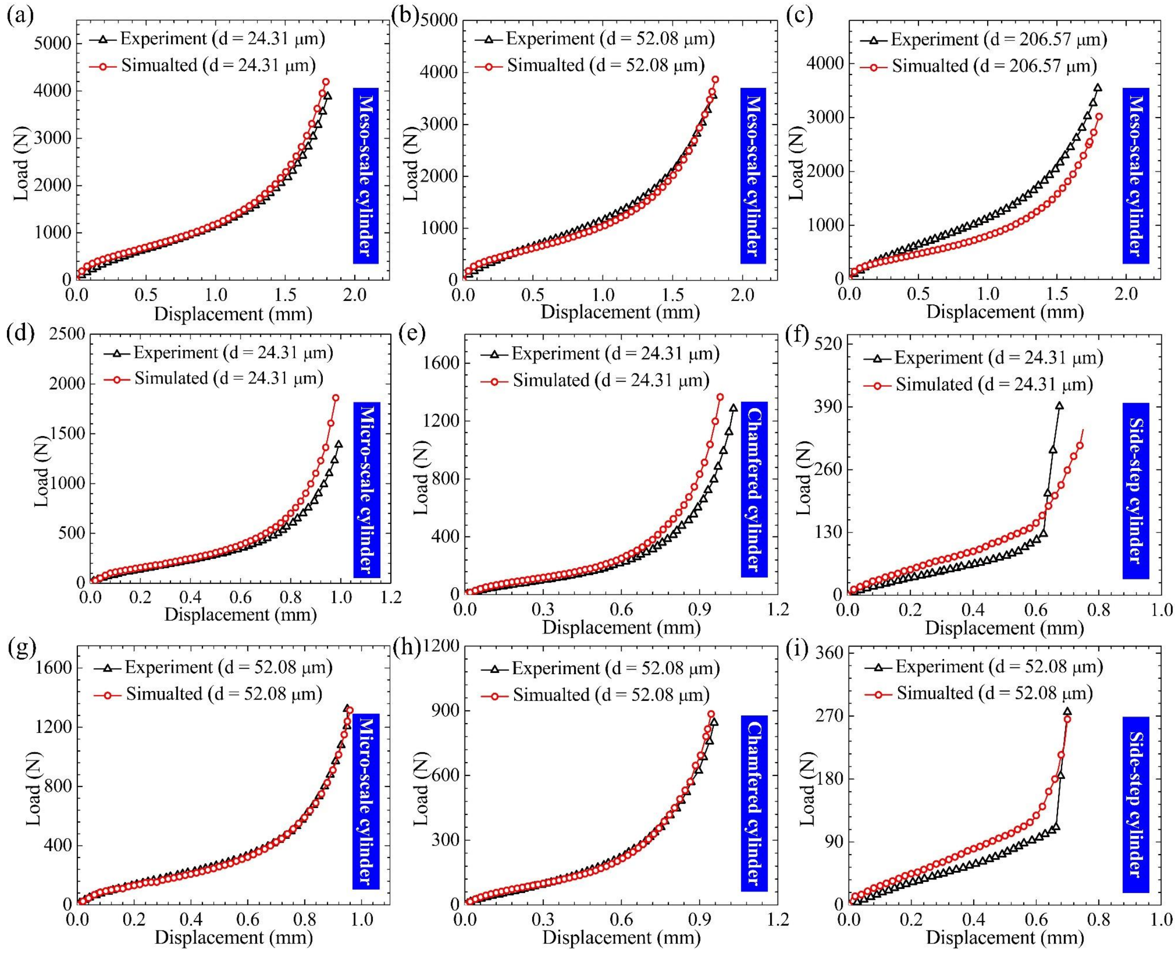

Fig. 10 Comparison of the load-displacement curves of simulation and those of physical experimentation using the cylindrical samples. (a)-(c) Meso-scale; (d) and (g) Micro-scale; (e) and (h) Chamfered; (f) and (i) Side-step cylinders.

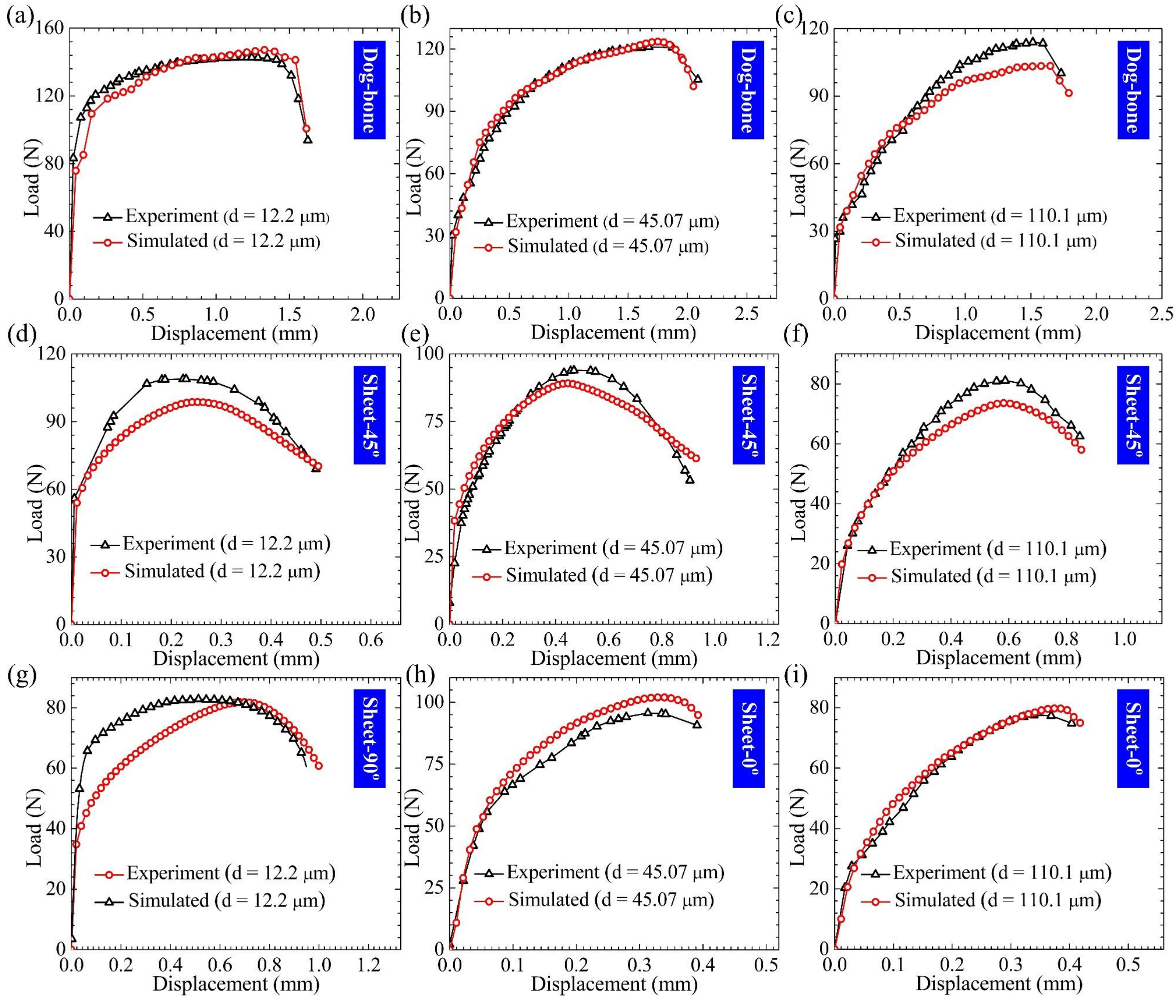

Fig. 11 Comparison of the load-displacement curves of simulation and those of physical experimentation using the sheet samples. (a)-(c) Dog-bone; (d)-(f) Sheet-45°; (g) Sheet-90°; (h) and (i) Sheet-0°.

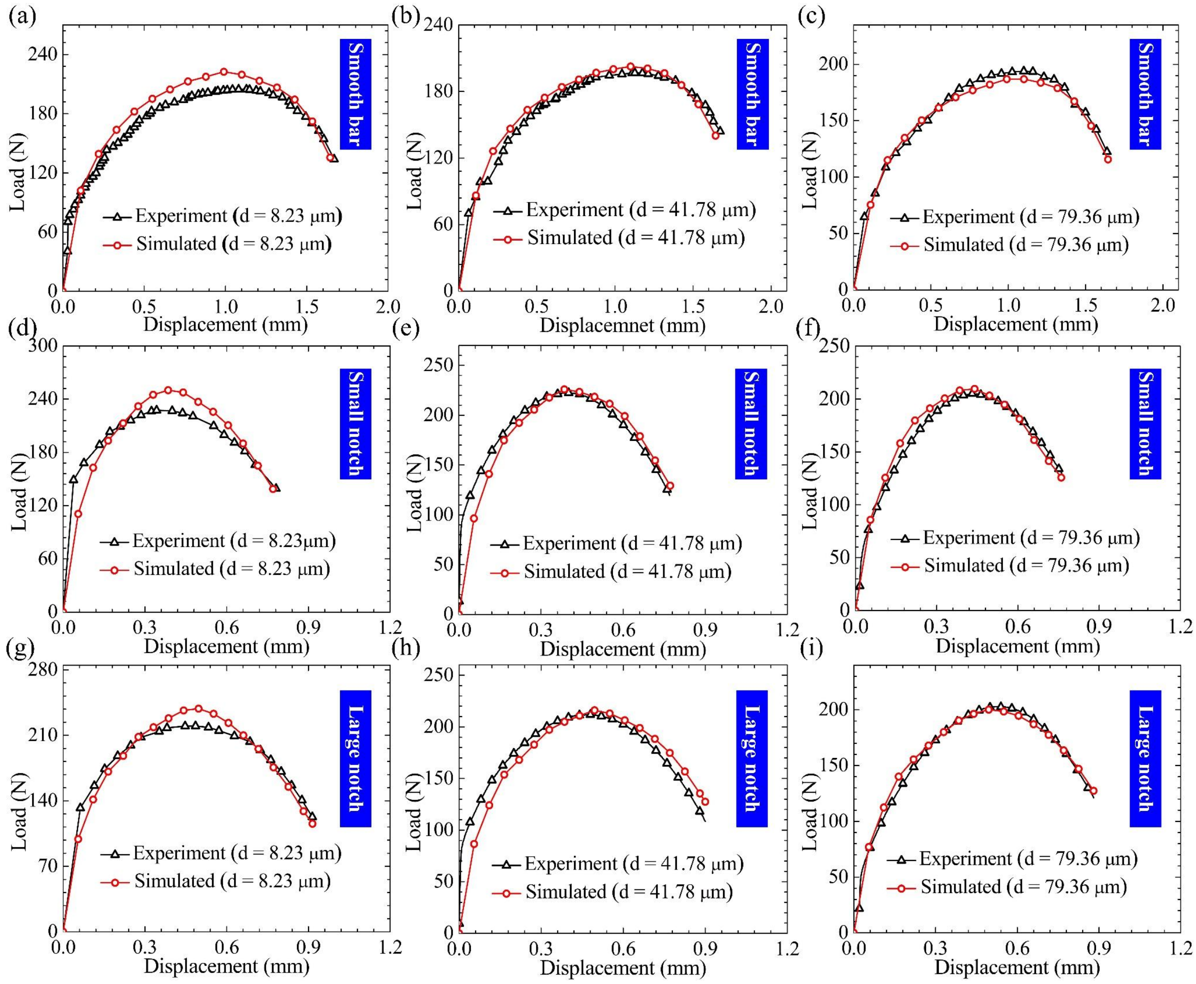

Fig. 12 Comparison of the load-displacement curves of simulation and those of physical experimentation using the round bar samples (Li et al., 2017). (a)-(c) Smooth bar; (d)-(f) Small notch and (g)-(i) Large notch.

4.2 Interactive effect of stress state and grain size on fracture behaviour and mechanism

The interactive influence of the grain size, the normalised third deviatoric stress invariant ξ and the stress triaxiality η on ductile fracture is studied. The parameters η and ξ are designated as follows:

$$\eta = \frac{\sigma_m}{\overline{\sigma}} \tag{11}$$

where $\sigma_m = \frac{1}{3}(\sigma_1 + \sigma_2 + \sigma_3)$ is the mean stress, and $\overline{\sigma} = \sqrt{\frac{1}{2}((\sigma_1 - \sigma_2)^2 + (\sigma_1 - \sigma_3)^2 + (\sigma_2 - \sigma_3)^2)}$ is the equivalent von Mises stress.

$$\xi = \left(\frac{r}{\bar{\sigma}}\right)^3 \tag{12}$$

In Eq. (12), $r = \left(\frac{27}{2}(\sigma_1 - \sigma_m)(\sigma_2 - \sigma_m)(\sigma_3 - \sigma_m)\right)^{1/3}$ is related to the deviatoric stress tensor.

In the compression of a tiny cylinder, the displacement of fracture initiation is where the micro-scale crack occurs. In tension experiments, the fracture displacement is determined based on an obvious decrease in load or the occurrence of micro-cracks observed via analyses of images taken by a digital camera to record the entire deformation process. In this study, fracture strain in fracture displacement is represented by the maximum equivalent plastic strain.

Fig. 13 reveals the evolutions of parameters η and ξ at the fracture initiation point. The average values of these two parameters are designated by Eqs. (13) and (14), respectively, in the following:

$$\eta_{avg} = \frac{1}{\bar{\varepsilon}_f^p}\int_0^{\bar{\varepsilon}_f^p} \eta\left(\bar{\varepsilon}^p\right) d\bar{\varepsilon}^p \tag{13}$$

where η_{avg} is the average stress triaxiality; $\bar{\varepsilon}^p$ is the equivalent plastic strain and $\bar{\varepsilon}_f^p$ is the equivalent plastic strain at the fracture displacement.

$$\xi_{avg} = \frac{1}{\bar{\varepsilon}_f^p}\int_0^{\bar{\varepsilon}_f^p} \xi\left(\bar{\varepsilon}^p\right) d\bar{\varepsilon}^p \tag{14}$$

where ξ_{avg} is the average normalised third invariant.

The average normalised third invariant and the average stress triaxiality are used in this study mainly because of the notable change in parameters ξ and η during the deformation process, especially in the compression and round bar tension experiments, which was also noted by Bao and Wierzbicki (2004). For the evolution of the stress state in compression, as shown in Figs. 13(a) and (b), parameters η and ξ generally decline as the grain size of the specimens with the same geometry increases. The stress state of sheet-45° exhibits a similar change with the grain size, as displayed in Fig. 13(c). For other specimens with the same geometry in Fig. 13(c) and (d), the normalised third invariant has a nearly constant value of 1, and the stress triaxiality fluctuates when the grain size increases.

According to Fig. 13, the interactive effect of the average stress triaxiality and the grain size on the fracture strain for each specimen is represented in Fig. 14. Fig. 14(b) clearly shows that the fracture strain of pure copper decreases as the stress triaxiality increases when the grain size remains constant during micro-scale compression and round bar tension deformations. However, the fracture strain increases with the stress triaxiality in sheet shear and tension deformations, as shown in Fig. 14(c). These different results are similar to those obtained by Bao and Wierzbicki (2004). To explain this influence of the stress state on the fracture strain, Fig. 15 presents the SEM fractographs of different specimens with a constant grain size. Figs. 15(a) to (c) show that the dimples are larger on the fracture surfaces of smooth bar at a low stress triaxiality and small notch at a high stress triaxiality. The increased stress triaxiality accelerates the voids' growth and coalescence, thus leading to a decrease in the fracture strain. In sheet specimens with a constant grain size, as shown in Figs. 15(d) to (f), dimple-dominant fracture with a flat-dimple necking mechanism occurs at $\eta = 0.48$ and $\xi = 0.99$ for sheet-0°, whilst shear-dominant fracture with an inter-void shearing mechanism occurs at $\eta = 0.06$ and $\xi = 0.56$ for sheet-90°. Mixed shear-dominant and dimple-dominant fracture occurs at the transition region for sheet-45°. The change in the fracture mechanism from inter-void shearing to necking mechanisms can thus explain the phenomenon in which the fracture strain increases with the stress state.

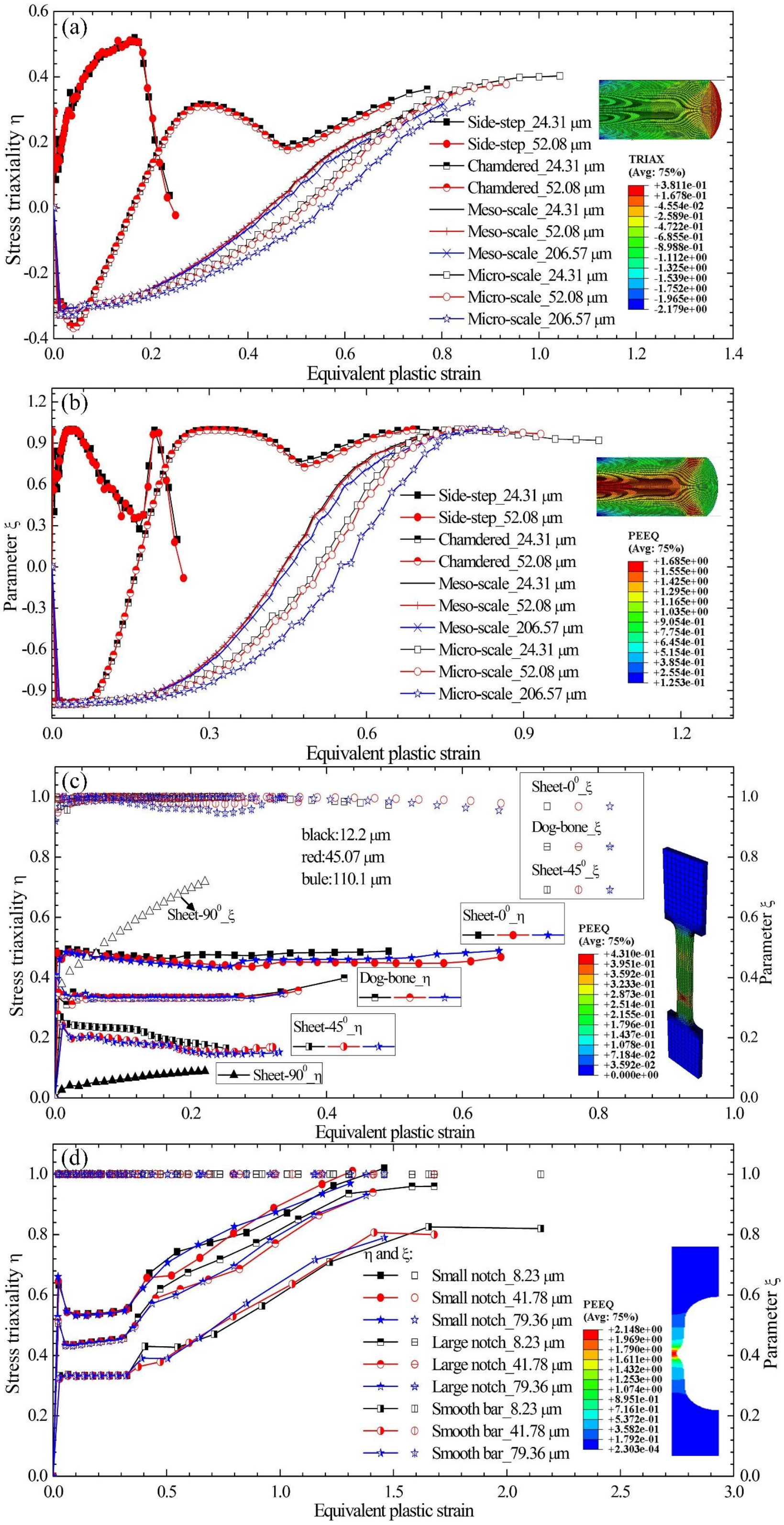

Fig. 13 Evolution of the stress state at the fracture initiation point of specimens. (a) and (b) Cylinder; (c) Sheet metal; and (d) Round bar specimens.

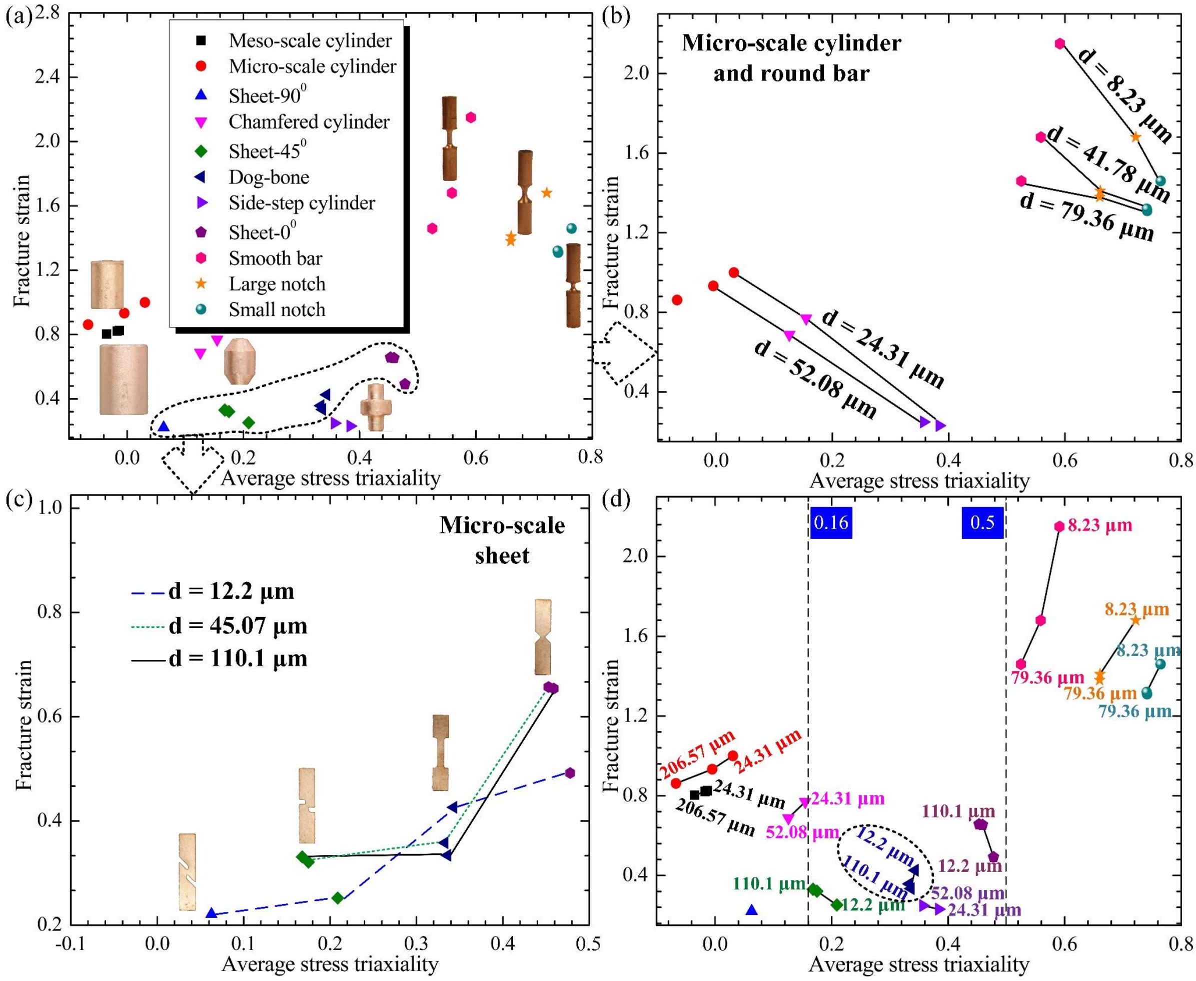

Fig. 14 Interactive influence of the average stress triaxiality and the grain size on fracture. (a) Full view; Specified grain size for (b) compression and round bar specimens; and (c) sheet specimens; (d) Specified shape specimens.

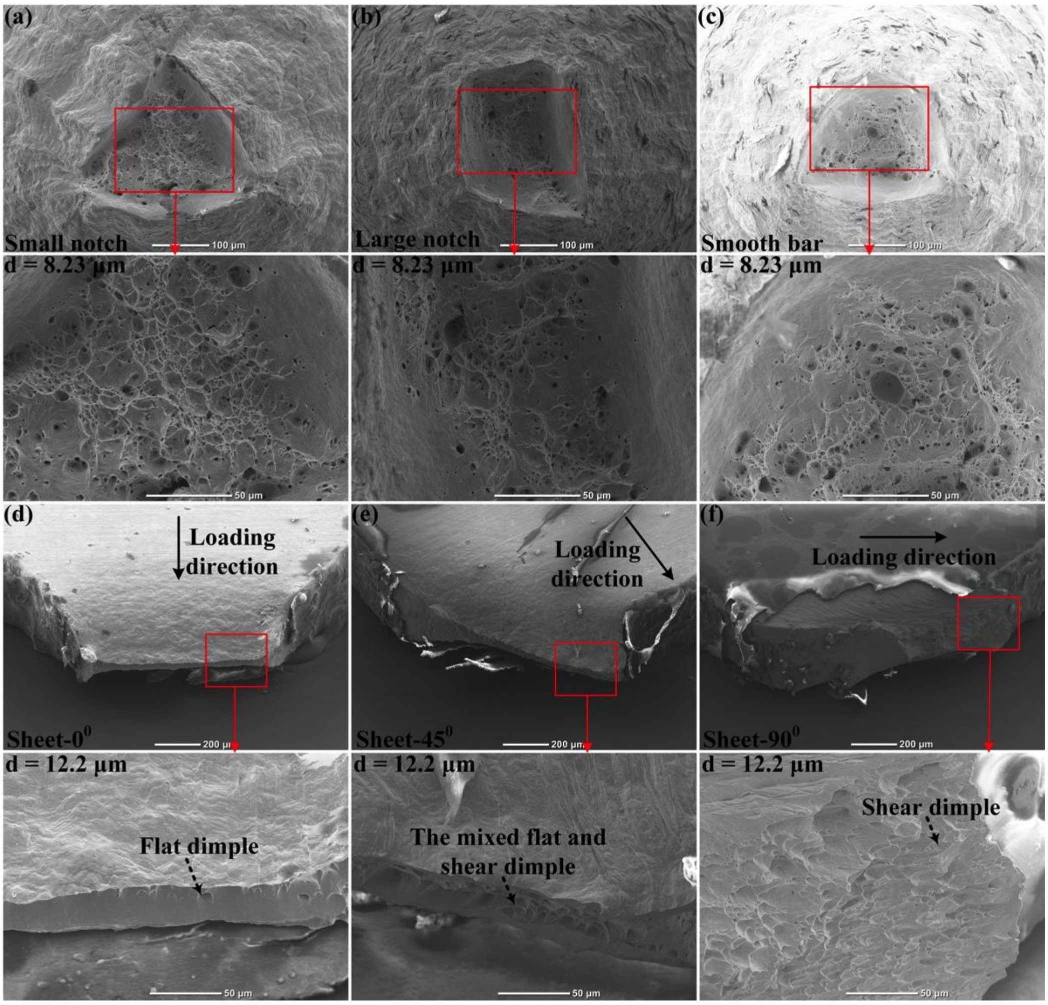

Fig. 15 SEM fractographs of round and sheet specimens with different geometries. (a) Small notch; (b) Large notch; (c) Smooth notch; (d) Sheet-0°; (e) Sheet-45°; and (f) Sheet-90°.

In addition, Fig. 14(d) shows that when the stress triaxiality is less than 0.16 or greater than 0.5, the fracture strain increases as the grain size decreases, whilst in this study the fracture strain decreases when the stress triaxiality lies between 0.16 and 0.5, except for the dog-bone sheet specimen. This exception may be a result of the constant normalised third invariant of dog-bone specimen, viz., 1, which differs from the values of other sheet specimens with different grain sizes. Furthermore, greater fracture strain occurs in the micro-scale cylinder than in the meso-scale cylinder when the grain size remains constant, as reported by Ran et al. (2013).

To further explore the influence of the grain size on the stress state, Fig. 16 represents the interactive relationship amongst the grain size, the average normalised third invariant and the average stress triaxiality. In Fig. 16(a), the stress triaxiality for each case and parameter ξ for the compression, sheet-45° and sheet-0° specimens decline as the grain size increases. The stress triaxiality increases with parameter ξ when the grain size remains constant in the compression and sheet shear and tension experiments, as shown in Fig. 16(b).

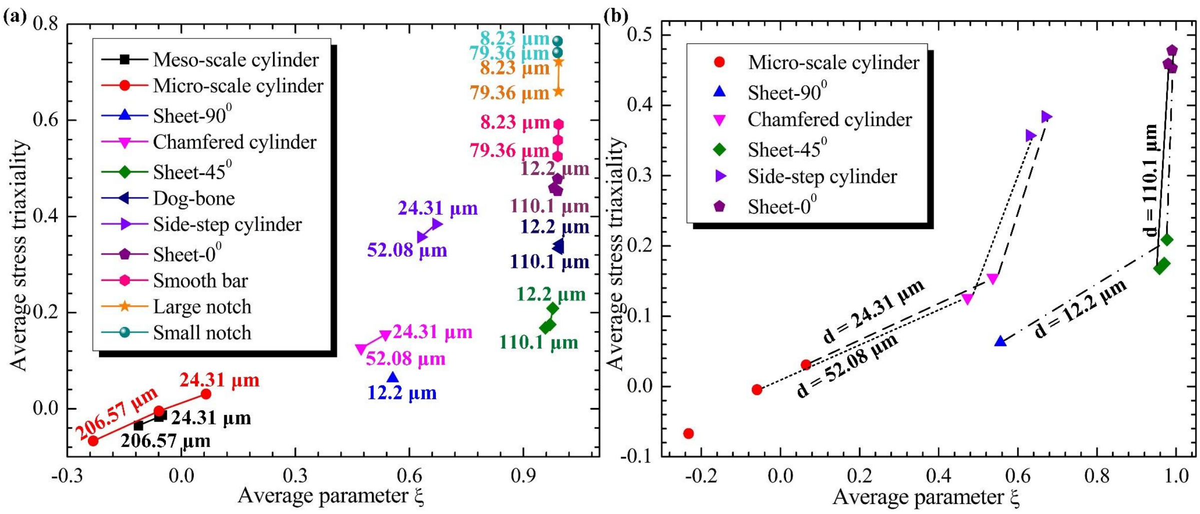

Fig. 16 Interactive relationship amongst the grain size, the average normalised third invariant ξ and the average stress triaxiality. (a) Full view; (b) Specified grain size for compression and sheet specimens.

The phenomenon in which a larger grain size causes a decline in the stress triaxiality can be explained by the fractured morphologies of small notch and dog-bone samples with various grain sizes, as presented in Fig. 17. Fewer voids, more uneven distribution of voids and deeper large dimples in localisation deformation are observed, and shear fracture dominates to an increasing degree when the grain size increases. It has been reported that dimple-dominant fracture with an inter-void necking mechanism and shear-dominant fracture with an inter-void shearing mechanism dominate in conditions of high and low stress triaxiality, respectively (Barsoum and Faleskog, 2007a). Hence, the increasingly dominant shear fracture indicates the lower stress triaxiality of specimens with a constant shape when the grain size is larger.

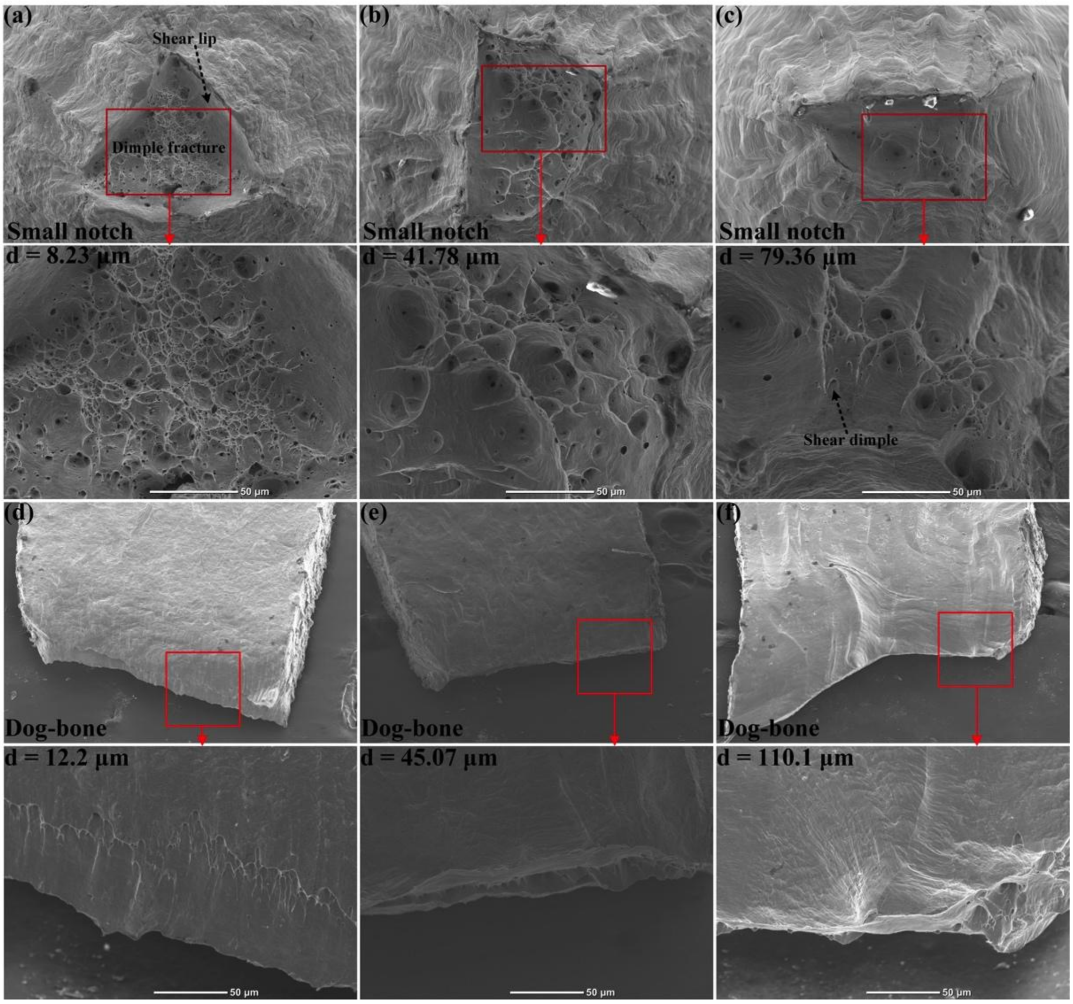

Fig. 17 SEM fractographs of small notch (Li et al., 2017) and dog-bone specimens with various grain sizes (μm). (a) 8.23; (b) 41.78; (c) 79.36; (d) 12.2; (e) 45.07; and (f) 110.1.

Generally, stress concentration occurs in the grain boundary and inclusions, which hinders the movement of dislocations to facilitate the nucleation of micro-voids. For specimens with a larger microstructural grain size and the same geometry, the fraction of GB reduces, leading to fewer micro-voids. Xu et al. (2015b) also stated that a larger grain size causes a decrease in micro-voids and facilitates the occurrence of void coalescence. In addition to the influence of the grain size on the evolution of void, the grain size affects the localisation deformation of the material and further facilitates failure. Fig. 18 shows SEM fractographs of micro-scale cylinders with various grain sizes. It can be seen that oblique shear fractures appear on the circumferential surfaces in each case and that the localisation deformation grows severer as the grain size increases. The greatly inhomogeneous deformation of micro-scale cylinder with a larger grain size is caused mainly by the more uneven grain distribution with various grain orientations and properties and the increased fraction of surface grain with few constraints and easy deformation. These grains can rotate and slide along the grain boundary to cause uneven deformation. Therefore, the larger the grain size, the severer the localisation shows.

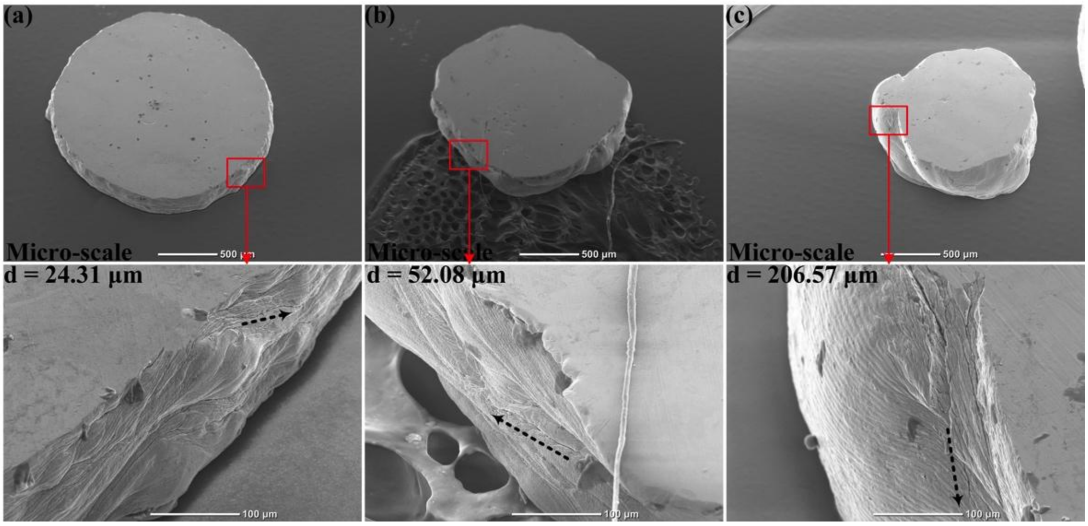

Fig. 18 SEM fractographs of micro-scale cylinder with various grain sizes (μm). (a) 24.31; (b) 52.08; (c) 206.57.

In addition to the interactive influence of the average stress triaxiality and microstructural grain size on fracture represented by the fracture strain, Fig. 19 shows the interactive effect of the average normalised third invariant and the grain size on fracture for each specimen. The average normalised third invariant almost has a constant value of 1 for dog-bone, smooth bar, large notch and small notch specimens with various grain sizes. When the grain size remains constant, the normalised third invariant causes a decrease in fracture strain during micro-scale compression experiments with cylindrical specimens, whilst the fracture strain is increased in the sheet shear and tension experiments using specimens of sheet-90°, sheet-45°and sheet-0°, as displayed in Figs. 19(b) and (c), respectively, similar to the influence of stress triaxiality on fracture behaviour. In specimens with a constant shape, both the normalised third invariant and the fracture strain decrease as the grain size increases in compression experiments for the values of parameter ξ below 0.56. However, the fracture strain increases, and the normalised third invariant shows a slight decrease at values of parameter ξ above 0.56 and below 1, as shown in Fig. 19(d).

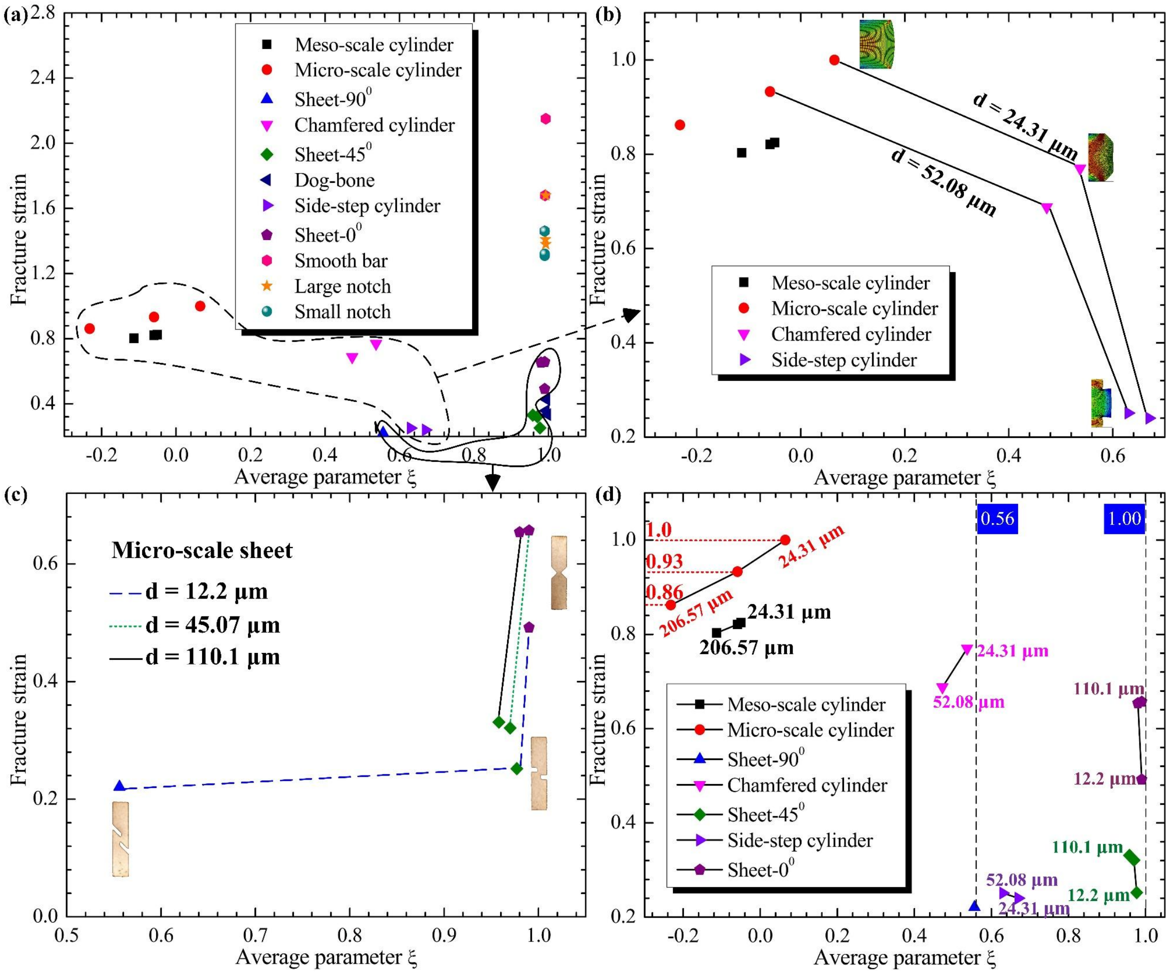

Fig. 19 Interactive effect of the average normalised third invariant ξ and the grain size on fracture: (a) Full view; Specified grain size for (b) compression specimens and (c) sheet specimens; (d) Specified shape specimens.

Figs. 14 and 19 reveal that ductility increases with a larger grain size when the normalised third deviatoric stress invariant and the stress triaxiality lie between 0.56 and 1, and between 0.16 and 0.5, respectively. However, the ductility of the material is better with a smaller grain size in other cases. A larger grain size generates fewer micro-voids, more uneven grain distribution and severer localisation deformation, which accelerates fracture failure. Furthermore, it causes a decrease in the stress triaxiality and a decline in the normalised third invariant at a low stress triaxiality below 0.5, which in turn affects the occurrence of fracture. These effects coexist and compete to increase ductility with a larger grain size for side-step cylinder, sheet-0° and sheet-45°, whilst ductility decreases for other specimens in this study. Furthermore, a higher stress state causes greater fracture strain when the sheet shear deformation changes to sheet tension deformation mainly due to the change from shear-dominant fracture with an inter-void shearing mechanism to dimple-dominant fracture with an inter-void necking mechanism. It is concluded that with a combination of the influences of stress state and grain size, a larger grain size and a higher stress state induce greater fracture strain in sheet specimens with fracture modes from shear-dominant to dimple-dominant. However, a smaller grain size and a lower stress state increase the fracture strain in other cases.

5. Conclusions

This study conducts tension, shear and compression experiments with micro-scale round, sheet and cylindrical samples with various grain sizes and geometries to examine the interactive influence of stress state and grain size on fracture behaviour as represented by fracture strain in μ-deformation, and corresponding simulations are performed with the combined constitutive model. The effects of the grain size and the stress state on fracture mechanism, mode and behaviour are analysed via observation of SEM fractographs. The following conclusions are drawn:

1. The combined surface layer and grain boundary strengthening constitutive model which assumes the material consists of SG, GI and GB, is constructed for various stress states and validated by meso-scale and micro-scale compression, shear and tension deformations of pure copper.

2. The interactive influence of the stress state and grain size on ductile fracture in μ-deformation is established. In specimens with a constant shape, a larger grain size causes a decrease in stress triaxiality and a decline in the normalised third invariant at low stress triaxiality (below 0.5). A larger grain size increases the fracture strain at the stress triaxiality between 0.16 and 0.5 and the normalised third invariant above 0.56 and below 1, whilst it reduces fracture strain in other cases. The increase in stress triaxiality deceases the fracture

strain for round bar tension and cylindrical compression specimens with a constant grain size, whilst the opposite is observed for sheet specimens. Furthermore, the effect of the normalised third invariant with a value below 1 on the fracture strain is similar to that of stress triaxiality.

3. The influence of the stress state on fracture mechanism, mode and behaviour in micro-scale ductile fracture is explored. When the grain size remains constant, the increase in the stress state makes the micro-defects growth and coalescence accelerate, which leads to a decrease in fracture strain for round bar tension specimens in the dimple-dominant fracture mode and for cylinder compression specimens in the shear-dominant fracture mode. However, the increase in the stress state causes an increase in fracture strain in the sheet shear and tension experiments. This result can be explained by the transformation of the fracture mechanism caused by inter-void shearing at a low stress state to inter-void necking at a high stress state.

4. The grain size affects the ductile fracture by influencing void nucleation, deformation behaviour and the stress state. Fewer micro-voids occur on the surface of the fracture, mainly because the fraction of the grain boundary at which void easily nucleates decreases as the grain size increases. The inhomogeneous deformation of specimens with a larger grain size is severer, mainly due to the increased fraction of the surface grain with few constraints and easy deformation and to the more uneven grain distribution with different grain orientations and properties. Localised deformation is significantly concentrated, and fracture thus more easily occurs. Furthermore, stress triaxiality and the normalised third deviatoric stress invariant at a low stress triaxiality decline with a larger grain size, which affects failure. These effects coexist and compete. Therefore, in this study the ductility increases with the increase in the grain size for side-step cylinder, sheet-0° and sheet-45°, whilst it decreases for other specimens with a constant shape.

5. Based on the interactive influences of the stress state and the grain size, a larger grain size and a higher stress state induce greater fracture strain in sheet specimens with fracture modes from shear-dominant to dimple-dominant. However, a smaller grain size and a lower stress state increase the fracture strain in other cases.

Acknowledgements

The authors would like to acknowledge the funding support to this research from the project of 152792/ 16E (B-Q55M) from the General Research Fund of Hong Kong Government and the project of No. 51575465 from the National Natural Science Foundation of China.

References

Bai, Y., Wierzbicki, T., 2008. A new model of metal plasticity and fracture with pressure and Lode dependence. International Journal of Plasticity 24, 1071-1096.

Ban, H., Yao, Y., Chen, S., Fang, D., 2017. The coupling effect of size and damage in micro-scale metallic materials. International Journal of Plasticity 95, 251-263.

Bao, Y., Wierzbicki, T., 2004. On fracture locus in the equivalent strain and stress triaxiality space. International Journal of Mechanical Sciences 46, 81-98.

Barsoum, I., Faleskog, J., 2007a. Rupture mechanisms in combined tension and shear—Experiments. International Journal of Solids and Structures 44, 1768-1786.

Barsoum, I., Faleskog, J., 2007b. Rupture mechanisms in combined tension and shear—Micromechanics. International Journal of Solids and Structures 44, 5481-5498.

Brünig, M., Gerke, S., Hagenbrock, V., 2013. Micro-mechanical studies on the effect of the stress triaxiality and the Lode parameter on ductile damage. International Journal of Plasticity 50, 49-65.

Brünig, M., Gerke, S., Schmidt, M., 2018. Damage and failure at negative stress triaxialities: Experiments, modeling and numerical simulations. International Journal of Plasticity 102, 70-82.

Chan, W.L., Fu, M.W., Yang, B., 2012. Experimental studies of the size effect affected microscale plastic deformation in micro upsetting process. Materials Science and Engineering: A 534, 374-383.

Clausen, B., Lorentzen, T., Leffers, T., 1998. Self-consistent modelling of the plastic deformation of f.c.c polycrystals and its implocation for diffraction mearsurements of internal stresses. Acta Materialia 46, 3087-3098.

Fu, M.W., Chan, W.L., 2012. A review on the state-of-the-art microforming technologies. The

International Journal of Advanced Manufacturing Technology 67, 2411-2437.

Fu, M.W., Wang, J.L., Korsunsky, A.M., 2016. A review of geometrical and microstructural size effects in micro-scale deformation processing of metallic alloy components. International Journal of Machine Tools and Manufacture 109, 94-125.

Furushima, T., Tsunezaki, H., Manabe, K.-i., Alexsandrov, S., 2014. Ductile fracture and free surface roughening behaviors of pure copper foils for micro/meso-scale forming. International Journal of Machine Tools and Manufacture 76, 34-48.

Gao, X., Zhang, G., Roe, C., 2009. A Study on the Effect of the Stress State on Ductile Fracture. International Journal of Damage Mechanics 19, 75-94.

Gurson, A.L., 1977. Continuum Theory of Ductile Rupture by Void Nucleation and Growth: Part 1 —Yield Criteria and Flow Rules for Porous Ductile Media. Journal of Engineering Materials and Technology 99, 2-15.

Jiang, B., Weng, G.J., 2004a. A generalized self-consistent polycrystal model for the yield strength of nanocrystalline materials. Journal of the Mechanics and Physics of Solids 52, 1125-1149.

Jiang, B., Weng, G.J., 2004b. A theory of compressive yield strength of nano-grained ceramics. International Journal of Plasticity 20, 2007-2026.

Keller, C., Hug, E., 2017. Kocks-Mecking analysis of the size effects on the mechanical behavior of nickel polycrystals. International Journal of Plasticity 98, 106-122.

Kim, G.-Y., Ni, J., Koç, M., 2007. Modeling of the Size Effects on the Behavior of Metals in Microscale Deformation Processes. Journal of Manufacturing Science and Engineering 129, 470.

Lai, X., Peng, L., Hu, P., Lan, S., Ni, J., 2008. Material behavior modelling in micro/meso-scale forming process with considering size/scale effects. Computational Materials Science 43, 1003-1009.

Li, H., Fu, M.W., Lu, J., Yang, H., 2011. Ductile fracture: Experiments and computations. International Journal of Plasticity 27, 147-180.

Li, W.T., Fu, M.W., Shi, S.Q., 2017. Study of deformation and ductile fracture behaviors in micro-scale deformation using a combined surface layer and grain boundary strengthening model. International Journal of Mechanical Sciences 131-132, 924-937.

Lou, Y., Huh, H., 2013. Prediction of ductile fracture for advanced high strength steel with a new criterion: Experiments and simulation. Journal of Materials Processing Technology 213, 1284-1302.

Lou, Y., Huh, H., Lim, S., Pack, K., 2012. New ductile fracture criterion for prediction of fracture forming limit diagrams of sheet metals. International Journal of Solids and Structures 49, 3605-3615.

McClintock, F.A., Kaplan, S.M., Berg, C.A., 1966. Ductile fracture by hole growth in shear bands. International Journal of Fracture Mechanics 2, 614–627.

Meng, B., Fu, M.W., Fu, C.M., Chen, K.S., 2015. Ductile fracture and deformation behavior in progressive microforming. Materials & Design 83, 14-25.

Meng, B., Zhang, Y.Y., Cheng, C., Han, J.Q., Wan, M., 2018. Effect of plastic anisotropy on microscale ductile fracture and microformability of stainless steel foil. International Journal of Mechanical Sciences 148, 620-635.

Meyersm, M.A., Ashworth, E., 1982. A model for the effect of grain size on the yield stress of metals. Philosophical Magazine A 46, 737-759.

Peng, L., Lai, X., Lee, H.-J., Song, J.-H., Ni, J., 2009. Analysis of micro/mesoscale sheet forming process with uniform size dependent material constitutive model. Materials Science and Engineering: A 526, 93-99.

Puttick, K.E., 1959. Ductile fracture in metals. Philosophical Magazine 4, 964-969.

Ran, J.Q., Fu, M.W., Chan, W.L., 2013. The influence of size effect on the ductile fracture in micro-scaled plastic deformation. International Journal of Plasticity 41, 65-81.

Teng, B., Wang, W., Xu, Y., 2017. Ductile fracture prediction in aluminium alloy 5A06 sheet forming based on GTN damage model. Engineering Fracture Mechanics 186, 242-254.

Vollertsen, F., Biermann, D., Hansen, H.N., Jawahir, I.S., Kuzman, K., 2009. Size effects in manufacturing of metallic components. CIRP Annals - Manufacturing Technology 58, 566-587.

Wierzbicki, T., Bao, Y., Lee, Y.-W., Bai, Y., 2005. Calibration and evaluation of seven fracture models. International Journal of Mechanical Sciences 47, 719-743.

Xu, J., Zhu, X., Shan, D., Guo, B., Langdon, T.G., 2015a. Effect of grain size and specimen dimensions on micro-forming of high purity aluminum. Materials Science and Engineering: A

646, 207-217.
Xu, Z.T., Peng, L.F., Fu, M.W., Lai, X.M., 2015b. Size effect affected formability of sheet metals in micro/meso scale plastic deformation: Experiment and modeling. International Journal of Plasticity 68, 34-54.
Yang, L., Lu, L., 2013. The influence of sample thickness on the tensile properties of pure Cu with different grain sizes. Scripta Materialia 69, 242-245.
Zhang, H., Dong, X., 2016. Experimental and numerical studies of coupling size effects on material behaviors of polycrystalline metallic foils in microscale plastic deformation. Materials Science and Engineering: A 658, 450-462.
Zhang, H., Liu, J., Sui, D., Cui, Z., Fu, M.W., 2018. Study of microstructural grain and geometric size effects on plastic heterogeneities at grain-level by using crystal plasticity modeling with high-fidelity representative microstructures. International Journal of Plasticity 100, 69-89.
Zhang, K.S., Bai, J.B., François, D., 2001. Numerical analysis of the influence of the lode parameter on void growth. International Journal of Solids and Structures 38, 5847-5856.
Zhou, J., Li, Z., Zhu, R., Li, Y., Zhang, Z., 2008. A mixtures-based model for the grain size dependent mechanical behavior of nanocrystalline materials. Journal of Materials Processing Technology 197, 325-336.
Zhu, R., Guilbert, E., Wong, M.S., 2016. Object-oriented tracking of the dynamic behavior of urban heat islands. International Journal of Geographical Information Science 31, 405-424.